Laser-based powder bed fusion thermal history of IN718 parts and metallurgical considerations

Mustafa Megahed[1],*, Martin Verhülsdonk[2], Simon Vervoort[2] and Paul Dionne[1]

[1] ESI Group, Research & Innovation, 45145 Essen, Germany

[2] Fraunhofer ILT, LPBF Application Development, 52074 Aachen, Germany

* Correspondence author; E-mail: Mustafa@Megahed.de.

Highlights:

- LB-PBF scan resolved modeling.

- Phase evolution during LB-PBF process.

- Influence of geometric features on LB-PBF thermal history.

- LB-PBF thermal modeling benchmark.

Abstract: Laser-based powder bed fusion (LB-PBF) as-built material properties; residual stresses and final component shape are dependent on the thermal history of the printed part. Design and optimization of the deposited material thus far depends on experimental trial and error. A systematic approach based on model informed optimization is missing; mainly due to the computational expense of resolving the scan path and performing the required transient simulations. In this work; the heat conduction equation is reformulated to enable accelerated simulations. The laser position and operating conditions are read from the build file. The laser trajectory throughout the component is resolved providing 3D temperature evolution. Simple demonstration parts exhibiting both hot and cold regions are used to induce different metallurgical responses of the deposited IN718. Thermocouples are used to validate calculated temperatures. CALPHAD based calculations utilize temperature predictions to obtain localized phase concentrations and predict the distribution of thermophysical properties throughout the build. Results are compared with hardness measurements confirming the accuracy of the overall modelling chain.

Keywords: additive manufacturing; thermal history; modeling; phase transformation; IN718; mechanical properties

1. Introduction

The scan strategy is known to influence material quality, properties, and morphology [1–7]. Optimization of the scan strategy, for example to avoid contour pores, is mostly a trial-and-error effort.

A modelling approach would immensely improve the efficiency of optimizing scan strategies and finding new strategies by which the temperature in overhangs can be managed, fine features can be accurately printed and the material microstructure can be controlled or graded as required by the final application. There are several numerical tools that analyze the energy distribution in L-PBF processes: FEM and CFD simulations have been used to analyze how defects occur and study the evolution of phase transformation and microstructures during solidification [6,8–12]. The need to resolve the relatively small spot size (~10^{-4} m) as well as the part scale (~10^{-1} m) require large computational efforts, that simulations are generally limited to small domains and a limited number of scan lines and layers.

Analytical tools such as the Rosenthal equation [13] and its Eagar & Tsai extension [14] are on the other hand suited for the analysis of single lines (hatches) and do not account for heat diffusion during laser off times. The predicted temperature distribution is usually used to obtain heat conduction mode melt pool dimensions [15–18]. In the keyhole regime, these models require extensions, usually considering the enthalpy of material as introduced by Hann *et al.* [19–21]. Alternatively, Liu *et al.* assumes that a keyhole is a black body allowing the use of a unit absorption coefficient. The absorption coefficient is dynamically calculated based on the relationship between melt pool width and its depth [22]. The higher the absorption coefficient, the deeper the melt pool showing the same trends of keyhole regime. The accuracy of melt pool predictions is not very high, but it is sufficient to support decisions on hatch spacing and layer thickness.

Ji *et al.* use the analytical solution of the Rosenthal equation in cylindrical coordinates to obtain the thermal history of the printed part [23]. A calibration factor is used to match the resulting melt pool shape to those observed experimentally. Heat diffusion during laser off periods (e.g., during recoating) was neglected, assuming that each layer has enough time to cool down to the initial temperature. It is thus not possible to account for skywriting, for example, which has a profound influence on melt pool dynamics [24] and the accumulation of heat due to changing part cross-sections and heights [25].

Wolfer *et al.* propose to solve the Eagar & Tsai equation to obtain the temperature during laser on time. The scan path is discretized and the energy of each segment, where the laser is on is added contributing to the heat source of the energy equation. Heat diffusion during laser off time is calculated using discrete convolutions [26]. The computational domain must be, however, rectangular. Whereas this is perfectly fine for study of scan patterns within the printed component, it would not readily lend itself to part scale analysis of complex shapes. Moran *et al.* propose solving the diffusion problem using finite element representation of the part and successfully demonstrated the coupling between analytic Rosenthal solution and FEM heat diffusion [25]. Switching the heat source off is represented by a negative solution of the Rosenthal solution. The implications of this approach on short laser off times and complete scan files (e.g., modulated laser, skywriting *etc.*) is not discussed. Mesh refinement near domain boundaries is required to correct the analytical solution to take adiabatic boundary condition into account.

Duong *et al.* demonstrated a solution coupling of a semi-analytic solution of the Eagar and Tsai equation with finite volume solution of the conduction equation to study L-PBF scan strategies. A qualitative verification was achieved by comparing predicted surface morphology with experimental images. The importance of accounting for skywriting and laser off periods was proven [24]. The research presented here is an extension of that work with a particular focus on the quantitative validation of the scan-resolved thermal model. Validated thermal histories are used to study phase transformations in

different regions of the printed specimens. The microstructures observed, and hardness measurements are correlated with the numerically predicted temperatures.

2. Thermal model

The model utilizes the semi-analytic solution of the Eagar and Tsai equation to characterize the heat input. The scan path is discretized, and multiple calculations are performed using an adequately fine time step to sum the heat input throughout the active laser scan time, which corresponds to the time step size utilized for the heat diffusion problem. A finite volume model accounts for arbitrary component shapes and uses the total amount of heat input during the last time step to calculate the heat diffusion throughout the material deposited and the base plate.

2.1. Eagar & Tsai

The Eagar & Tsai equation assumes a Gaussian distribution of the heat source [14]. In this study it is scaled by a material specific absorption coefficient. The temperature at a specified spatial location and time is obtained by evaluating a time integral; the non-dimensional form of which is given in Equation (1) [14]—see also Table 1. The peak temperature is capped at the alloy's boiling temperature.

$$\theta(X,Y,Z,t) = n\int_0^F \left(\frac{e^{-\frac{1}{2}\left(\frac{R_{xy}^2}{f+u^2}+\frac{z^2}{f}\right)}}{\sqrt{f}\left(f+u^2\right)} \right) df \tag{1}$$

$$n = \frac{Aqv_s}{4\pi\alpha^2\rho c_p\left(T_m-T_i\right)} \tag{2}$$

$$L_{ref} = 2\frac{\alpha}{v_s} \tag{3}$$

$$t_{ref} = \frac{L_{ref}}{v_s} \tag{4}$$

$$T_{ref} = \frac{\left(T_m-T_i\right)}{\sqrt{2\pi}} \tag{5}$$

Table 1. Nomenclature utilized for equations 1 to 6.

A	Absorption coefficient	-
a	Thermal diffusivity	m²/s
c_p	Specific heat	J/kg K
f	Non-dimensional time coordinate	-
F	Non-dimensional time at which we evaluate T	-
I_i	Integrand value at Gaussian point i	
L_{ref}	Reference length	m
l	Thermal conductivity	W/m K
M	Number of Gaussian integration points used to evaluate the integral over each sub-interval	
n	Operating parameter	
N	Number of scan path subintervals; these points cover the integration period $f = 0$ to $f = F$	
q	Laser power	W
Q_s	Surface heat source / boundary condition	W/m³
R_{xy}	Non-dimensional distance from heat source in the XY plane	-
r	Density	Kg/m³
t	Time	s

Table 1. *Cont.*

t_{ref}	Reference time	s
T	Temperature	K
T_i	Initial temperature	K
T_m	Melting temperature	K
T_{ref}	Reference temperature	K
Θ	Non-dimensional temperature increase above T_i	-
u	Non-dimensional laser Gaussian variance, A value of zero corresponds to a point source (Rosenthal eqn.)	-
v_s	Scan speed	m/s
w_i	Weight factor at Gauss point i	-
X, Y, Z	Dimensional location at which the temperature is desired at t	m
z	Non-dimensional distance in Z direction from the heat source	-

Note that R_{xy} is a function of *f*, which complicates the integral. Because of the complex form of the integral and the non-analytical relationship of *R(f)*, the integral must be evaluated numerically. Standard Gaussian integration is used. To obtain the temperature at the current non-dimensional time F, we integrate Equation (1) backwards along the laser scan path to the start point at *f* = 0. The integral is evaluated by breaking up the integration period (*f = 0* to *f = F*) into a series of smaller integration intervals and summing the integration results from the integration integrals. Defining the integrand as *I*, the numerical integral is expressed as:

$$\theta(X,Y,Z,t) = n\int_0^F I(R,f)df = \sum_{j=1}^N \int_{f_{j-1}}^{f_j} I(R,f)df = \sum_{j=1}^N \sum_{i=1}^M w_i I_i \qquad (6)$$

$$f_0 = 0, f_N = F, f_{j-1} < f_j$$

In Equation (6), *R* is a function of *f*, so the integrand could have been written as *I(f)* in Equation (6), but the dependence on the radius *R* is explicitly stated because of its importance. The inner summation on the RHS of Equation (6) is the standard Gaussian integration summation, and the outer summation is the sum over the integration intervals. In summary, referring to Equation (6), the period of integration (0 to F) is broken up into N integration intervals, and over each integration interval Gaussian integration is performed using M gauss points.

The concept behind Equation (6) is shown schematically in Figure 1 (left). We evaluate the temperature at point (X, Y, Z), Figure 1 (left) shows the contribution to the temperature from the integration intervals defined between the two red end points. The laser was at the left end point at time f_{n-1}, and at the right end point at time f_n. Three Gauss integration points are shown as the green points along the laser path (*M = 3* in Equation (6)). Each integration interval corresponds to one of the values of *j* in Equation (6) and is a subset of a longer laser scan. Values of *R* and *f* at the Gauss points needed to evaluate the integrand are interpolated linearly from the end point values.
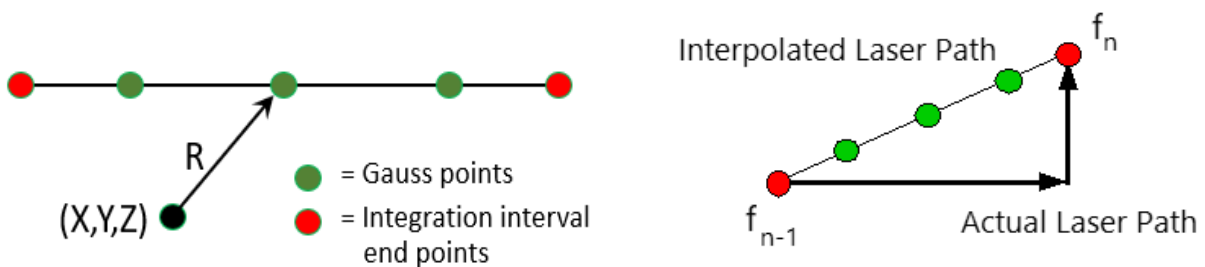
Figure 1. Integration Along Interval (left). Example of incorrect interpolated path (right).

Because of the linear interpolation used to calculate data at the Gauss points, the integration intervals may not be larger than a scan hatch. Figure 1 (right) shows an example of an integration interval scanning two or more hatches that are not colinear. The linear interpolation between the start and end points would yield wrong results.

Integration accuracy is influenced by the variation of the integrand over the integration interval, the size of the integration interval (f_n–f_{n-1}), and the number of Gauss points used (M) used to integrate over the integration interval. In general, more Gauss points are required for larger intervals (larger f_n–f_{n-1}), smaller distances (smaller R), and smaller times (smaller f). For some spatial locations (X, Y, Z) the integrand is highly non-linear for a small portion of the time and very benign for the remainder of the time. For other spatial locations the integrand is benign over the entire time. The integrand variation with time has both spatial and temporal influences and is a function both of how far the laser is from the point and how long ago it was at that position. We thus use non-uniform distribution of Gauss points; the integration interval (f_n–f_{n-1}) is small near $f = 0$ and increases as f gets larger. For the spatial definition, the number of Gauss points, M, is small for locations far away from the laser position and increases as we approach the laser position.

2.2. Heat diffusion

The heat conduction equation (Equation (7)) is solved to predict the evolution of thermal history during laser on (active heat source as defined by the solution of Equation (1)) and during laser off periods (pure energy diffusion). It is cast in a finite volume formulation; first order time stepping is utilized together with a pre-conditioned conjugate gradient solver to solve the problem. 20 iterations for each time step are usually enough to achieve convergence.

$$\rho c_p \frac{dT}{dt} = \nabla \cdot \left(\lambda \nabla T \right) + Q_s \tag{7}$$

The component side boundaries lose heat to the surrounding powder. A convective heat transfer coefficient of 4 W/m²·K is assumed. When designing the validation experiments, the base plate is foreseen to be isolated from the printer structure by powder. It is thus assumed that the base plate behaves similarly to the printed component. All boundary conditions can be however adapted to other configurations at no additional programming or computational cost.

A three-dimensional, unstructured adaptive Cartesian grid generator is used to discretize the parts' geometry and the base plate [27]. The most appealing property of a Cartesian grid is its efficiency in filling space with a minimum number of computational cells, given a certain grid resolution. A 2^n tree data structure is used allowing for arbitrary refinement and coarsening of the grid. In the case of LB-PBF we are interested in refinement in the XY plane only with the aim of capturing fine geometric features accurately. In build direction (Z-direction) the grid size is defined to correspond to the layer thickness or a multiple thereof. This allows us to avoid the need for a slicing tool, since the grid inherently resolves the printed layers. The combination of Cartesian and unstructured polyhedra allows for accurate representation of curved surfaces.

In this approach the Eagar & Tsai temperature field (solution of Equation (1) or its discretized version Equation (6)) is transferred to the finite volume solver in "chunks". This is done by breaking up the laser scan into a series of scan segments. Then, each scan segment provides an Eagar & Tsai solution that will be transferred to the finite volume solver and tracked as a coarse-scale solution (Figure 2).
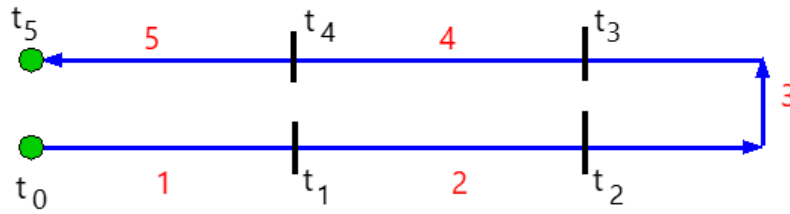
Figure 2. Laser Scan Broken into Scan Segments.

Note that these laser scan segments do not correspond to the integration intervals shown in Equation (6) and Figure 1. The integration intervals of Equation (6) are used to evaluate of the temporal integral of the Eagar & Tsai equation. The scan segments of Figure 2 define separate parts of the scan path covering the complete part volume and are transferred to finite volume solver to quantify the heat source.

In Figure 2 the laser starts in the lower left corner at time t_0 and finishes just above that location at time t_5. The laser path is broken up into five scan segments (numbered in red) defined by the internal times t_1 through t_4. Each of the five scan segments defines an Eagar & Tsai solution that is transferred to the finite volume solver. During the solution process, at the start of each finite volume scale time step the Eager & Tsai solver is queried if any of the solutions are to be transferred (there will be none for laser off time). The Eagar & Tsai solver will loop over the scan segments to determine what, if anything, is to be sent to the finite volume solver. There are three different cases that can be encountered:

- If the scan segment has already been transferred, it is skipped.
- If the scan segment has not been transferred but the current time is less than the segment transfer time, that solution is not transferred.
- If the scan segment has not been transferred and the current time is larger than the transfer time, then that solution is transferred to be tracked as a coarse scale solution, and the segment is marked as having been transferred.

The scan segments are defined using the finite volume (coarse) scale time step size, although the model is general enough to allow for different scan segment definitions.

2.3. Coupling between E&T and CFD

At any instant in time and at any spatial location, the temperature field is the sum of the Eagar & Tsai and the conduction equation solutions allowing quick calculations of the thermal field in the global domain. In theory the fine-scale solution will affect the temperatures throughout the part being printed, but in practice the effect is limited to a small volume close to the current laser position. At every time step, the laser location is defined by referencing the scan file. The corresponding process parameters are read from associated parameter files.

The Eagar & Tsai solver only requires an initial temperature as input to determine the temperature distribution in the vicinity of the laser. It is obtained from the finite volume model.

The scan paths can be defined using a CLI file [28], G-Code [29] or using a csv table of scan vectors defined manually for testing purposes. This study we performed using CLI files complimented with process parameters for each of the CLI files.

The Eagar & Tsai temperature field is calculated at the cell centers of the finite-volume grid using the numerical procedure described above and these temperatures are stored in a separate array. Thus,

each cell in the finite volume computational domain has two separate temperatures defined—a coarse scale temperature from the finite-volume solution and a fine-scale temperature from the Eagar & Tsai solution.

IN718 properties used throughout this study are summarized in Table 2.

Table 2. IN718 properties.

Property [Unit]	Semi-analytics model
Absorption coeff. [-]	0.53 [30]
Solidus [K]	1528 [31]
Liquidus [K]	1610 [31]
Latent heat of fusion [kJ/kg]	227 [32]
Boiling temperature [K]	3186
Latent heat of evaporation [kJ/kg]	7340 [33]
Density [kg/m^3]	8200 [32]
Thermal conductivity [W/m·K]	15 [32]
Specific heat [J/kg·K]	603 [32]

2.4. Model assessment

The semi-analytical model resolves all laser scans. Provided the printer and the scan files allow for dynamic adaptation of process parameters, the model should be able to resolve these changes accordingly.

The use of polyhdra cells allows for flexible representation of complex geometries. The user only needs to decide on the maximum cell size that would allow for the finest feature to be resolved. The grid generation is done automatically. Since layer heights can be very small (10–20 µm in height), particular care is needed when resolving the build direction. Resolving each layer does lead to very large computation grids. On the other hand, it is important to capture heat accumulation and dissipation accurately. Preliminary trials show that lumping up to 10 layers together still leads to acceptable results.

Modern multi-laser printers have not been considered yet. It is assumed that representing each laser by an instance of the Eagar & Tsai solver, each providing the heat source to a global CFD model, would account for all heat sources without increasing computational cost significantly. Beam shaping is an important parameter of new scan strategies. Non-Gaussian beams cannot be described using the Eagar and Tsai model and as such this model is not applicable when studying the effect of beam shaping on the thermal history, unless corresponding analytical solutions for different beam shapes are implemented. If corresponding analytical solutions are available, the numerical procedure detailed here can be used with the Eagar & Tsai solver replaced by the new solver.

3. Experiment

Experiments for validation are conducted on a customizable laboratory LB-PBF system. The machine features a single mode fiber laser with 400 W of laser power, a laser spot size of 110 µm, an F-Theta lens, a circular build plate of 110 mm and a thermal imaging camera. A polymer build plate adapter is used to hold the rectangular build plate made of IN718, measuring $92 \times 75 \times 10$ mm³. The polymer build plate holder is designed to isolate the build plate from the rest of the printer mass that cannot be described thermally. The polymer build plate holder is shown in Figure 3. The build plate is supported by 8 pointed screw tips, which theoretically have no conductivity due to the point contacts. The space below the base plate is filled with the same powder as that used in the process, hence isolating the base plate with a

layer having the same properties as the powder surrounding the part investigated. The heat flux is estimated to be reduced to less than 1% compared to the bulk metal [34].
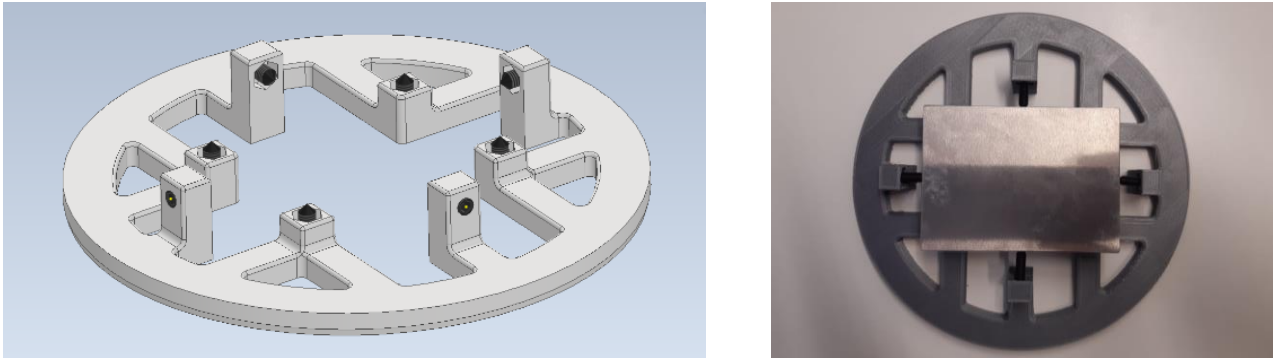
Figure 3. CAD of build plate adapter for reduced heat flux (left). Build plate adapter with mounted build plate (right).

Two cones are built, one is a standing cone with its base directly on the build plate hence providing good thermal connection to the build plate, which acts as a thermal sink. The second cone is inverted with its top tip connected to the base plate. The very small connecting interface area restricts the flow of heat to the base plate. Figure 4 shows the CAD model of the build plate and both cones. Several thermocouples of type K, NiCr-Ni with a diameter of 0,1 mm diameter are connected to the top side of the build plate to provide quantitative temperature measurements during the build process in addition to the thermal images acquired by the infrared camera. The thermocouples are connected to Pico USB TC-08 Thermologger operating at 10 Hz.

The cone dimensions, their positions on the build plate as well as the position of the thermocouples are also documented in Figure 4. It is worth noting that the standing cone is slightly different than the inverted one as a tunnel was designed to accommodate the thermocouple wiring that reaches to the center of the standing cone.
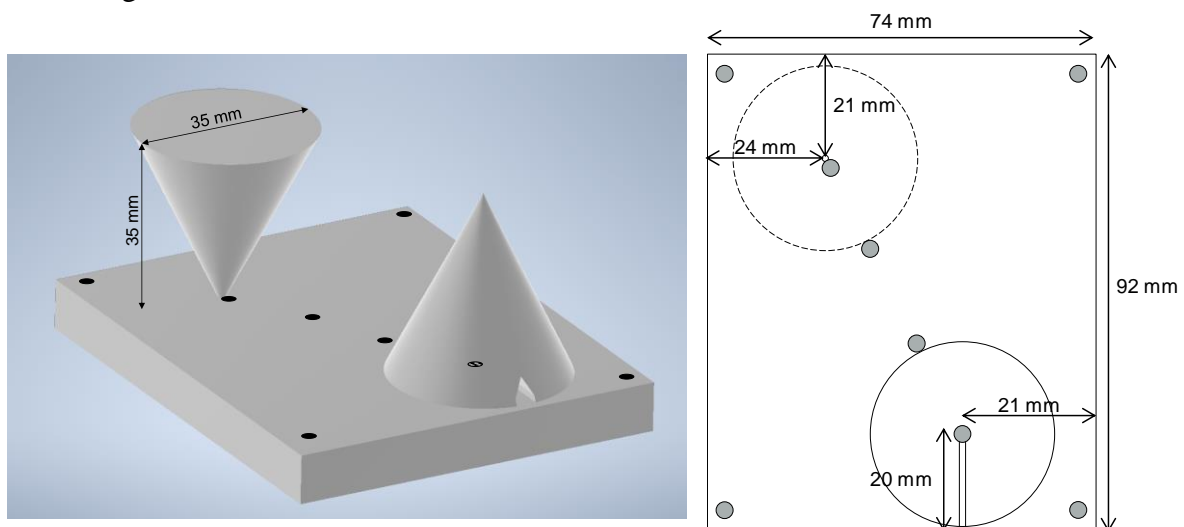
Figure 4. Standing and inverted cone specimens as well as position of thermocouples installed on the build plate. All dimensions are provided in millimetres.

IN718 is used for this experiment. Figure 5 shows an example SEM and hollow particle images of the powder showing mostly spherical particles with very little porosity. The volumetric powder size distribution is shown in Figure 6 where D10, D50 and D90 are quantified to be 20.58 µm, 32.27 µm and 47.09 µm, respectively.
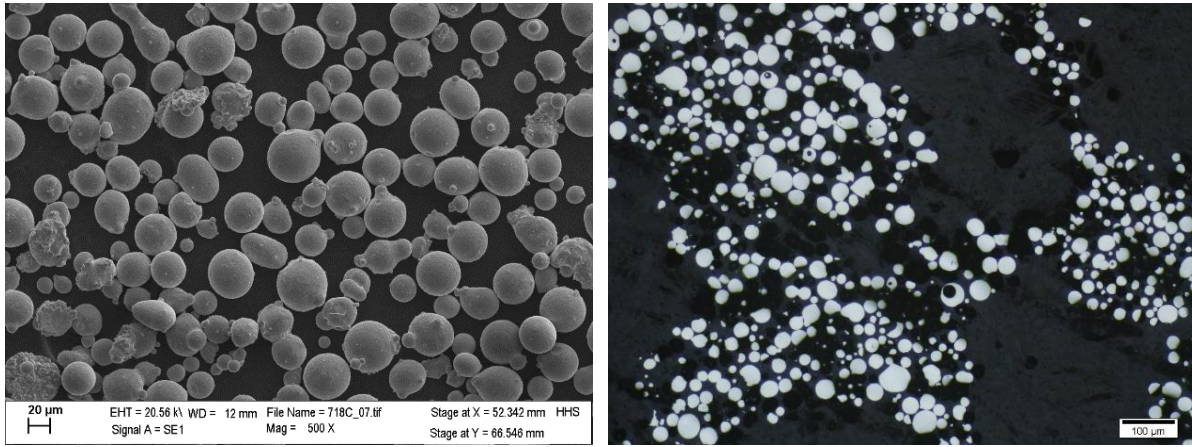
Figure 5. IN718 powder SEM image (left) and hollow particle image (right) showing mostly spherical particles with very few satellites and hardly any particle porosity.
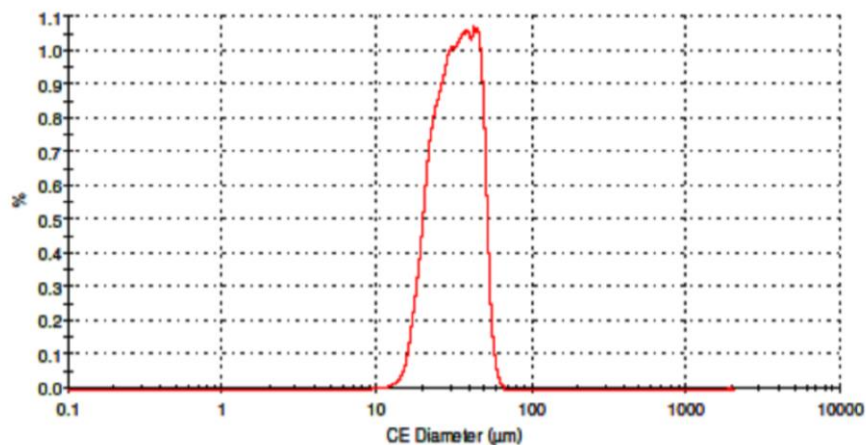
Figure 6. Volumetric powder size distribution: D10 = 20.58 µm, D50 = 32.27 µm and D90 = 47.09 µm.

The specimens are manufactured with a scanning velocity of 960 mm/s, a laser power of 180 W, and a hatch distance of 100 µm with an alternating layer rotation of 90° at a layer height of 30 µm. The spot diameter is 110 µm.

As-built Vickers hardness is measured at several points throughout the central section of the standing and inverted cones. according to ISO 6507-1. The indentation points are 1 mm apart. The mean value and the standard deviations are calculated from several measurements. The specimens are then polished and etched with an alcoholic solution in preparation of SEM imaging.

4. Results and discussion

A polished and etched cross-section of the resulting material is displayed in Figure 7, showing minimum porosity and the typical fish scale structure of overlapping melt pools. The relative density of the

deposited material is 99.8%. The melt pool dimensions cannot be extracted from Figure 7 because of the hatch spacing used and the overlapping of the melt pools. It can be, however, seen that conduction mode melting is dominant with relatively flat melt pools throughout the image.
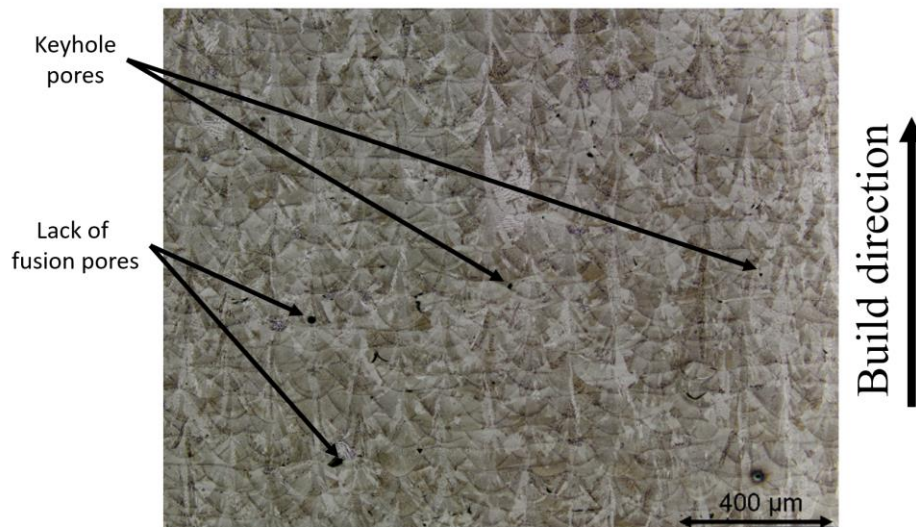
Figure 7. Polished and etched cross section of standing cone specimen. Example defects like lack of fusion and keyhole pores are shown.

The temperature evolution in both cones is very different due to the significant difference in the corresponding connecting area between cone and the base plate. Figure 8 shows a sequence of captured thermal emissions during printing. Higher emissions result from higher temperatures. Comparing the emission intensity thus indicates the relative thermal energies registered for each of the cones. The inverted cone is printed on the upper left corner of the image, the standing cone is positioned to its right. The first two images were taken at the beginning of the printing process, the last two towards the end. The estimated average temperature by the infrared camera system is also provided on the upper right side of the images. The average temperature registered increases with time and then decreases again at the end of the print job. During printing the thermal emissions of the inverted cone are significantly higher than those captured for the standing cone, which is mostly invisible (see images 1 and 3 in Figure 8) apart from single scan lines that show higher emissions that are directly dissipated to the base plate (see images 2 and 4 in Figure 8).

In a preliminary verification of the model predictions Figure 9 shows contour plots of the temperature evolution for both cones. The setup starts at uniform atmospheric conditions (no preheating was applied). During first layers the cones do not exhibit large differences in their temperatures (this is not directly comparable with the emission images showing the emissions inside the cones). As the cones build progresses the skin temperature shows a significant heat-up of the inverted cone as compared to the standing cone. Towards the end of the print job the skin temperature difference is in the order of 400 K, similar to the estimates obtained from thermal emission images (Figure 8; (1) compared to (3)). The accumulation of heat in the inverted cone is due to the constriction of heat transfer cross section, which hinders the dissipation of process energy to the base plate.
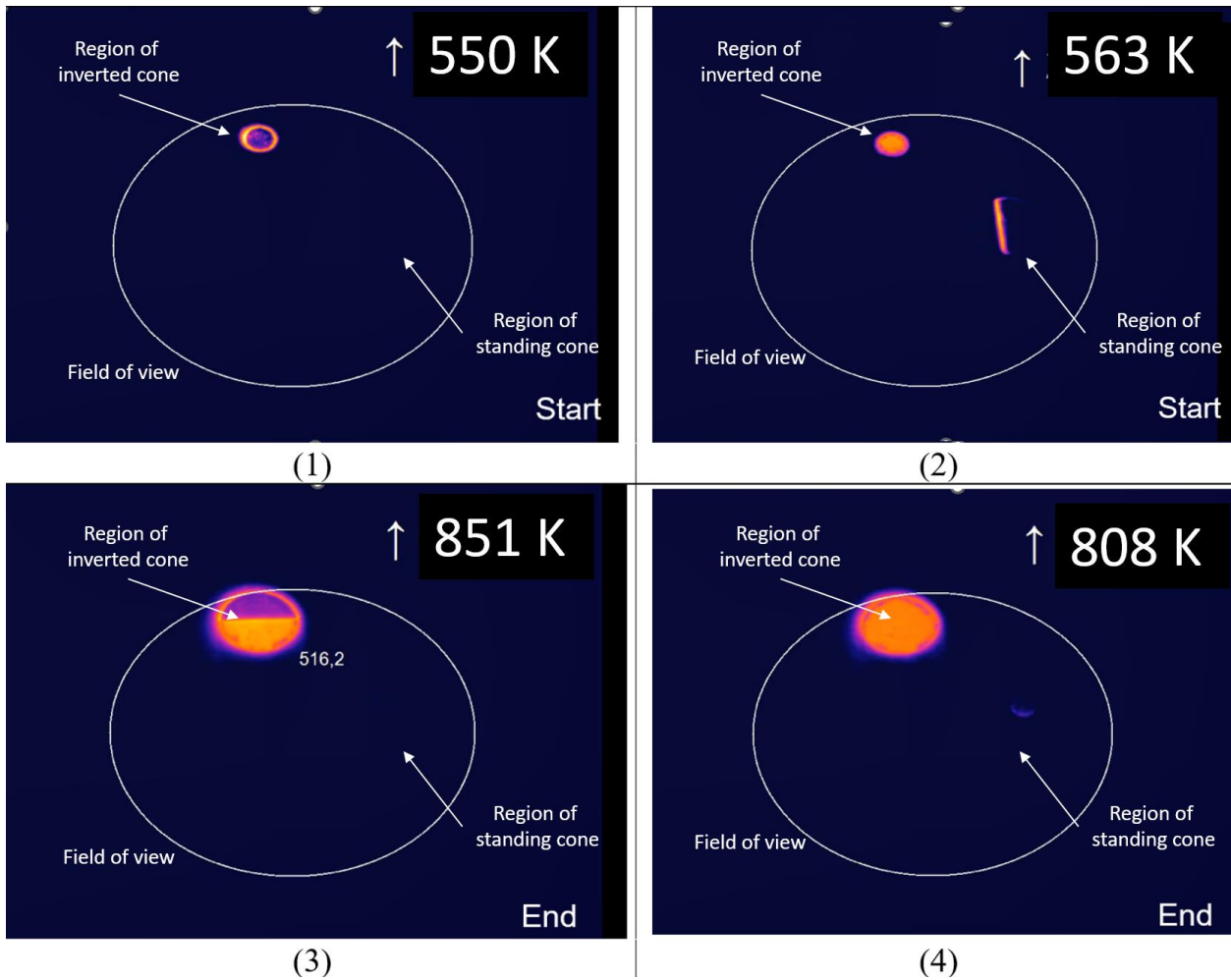
Figure 8. Sequence of infrared images showing estimated temperature levels of processed layers. The moment of exposure of the inverted cone is shown on the left (1: Start, 3: End), the one of the standing cone on the right(2: Start, 4: End). The exposure of the standing cone at the start (2) can be seen as a line, due to high cooling rates, while the after glow of the inverted cone is still visible in the same image. The exposure of the standing cone at the end (4) can bare be seen. The estimated average temperature is printing in the upper right side of each image.

The thermocouple readings provide a quantitative validation of the numerically predicted temperatures. Figure 10 compares thermocouple 5 and 8 readings as compared to predictions at monitor points placed at same position as the thermocouples. Exposure is started at t = 0 s. Point 5 is placed very close to the "top" of the inverted cone and point 8 is placed at the center of the standing cone, in the tunnel foreseen for the thermocouple wires. For both points, the temperature increases relatively quickly as the laser approaches the thermocouples/monitor points reaching a maximum when the laser is in direct vicinity. As more layers are deposited and the laser moves further away, the temperature decreases. After approximately 3.5 hours (12,770 s) printing is concluded, the laser is switched off and the build cools down at a higher rate.

Point 5, close to the inverted cone, does not cool down as quickly as point 8 and remains hotter for a longer period as per the energy accumulated in the inverted cone. Point 8, on the other hand, shows how process energy is quickly dissipated cooling the overall cone geometry at a higher rate than that of the inverted cone. The numerical predictions show a very good agreement with the measurements.
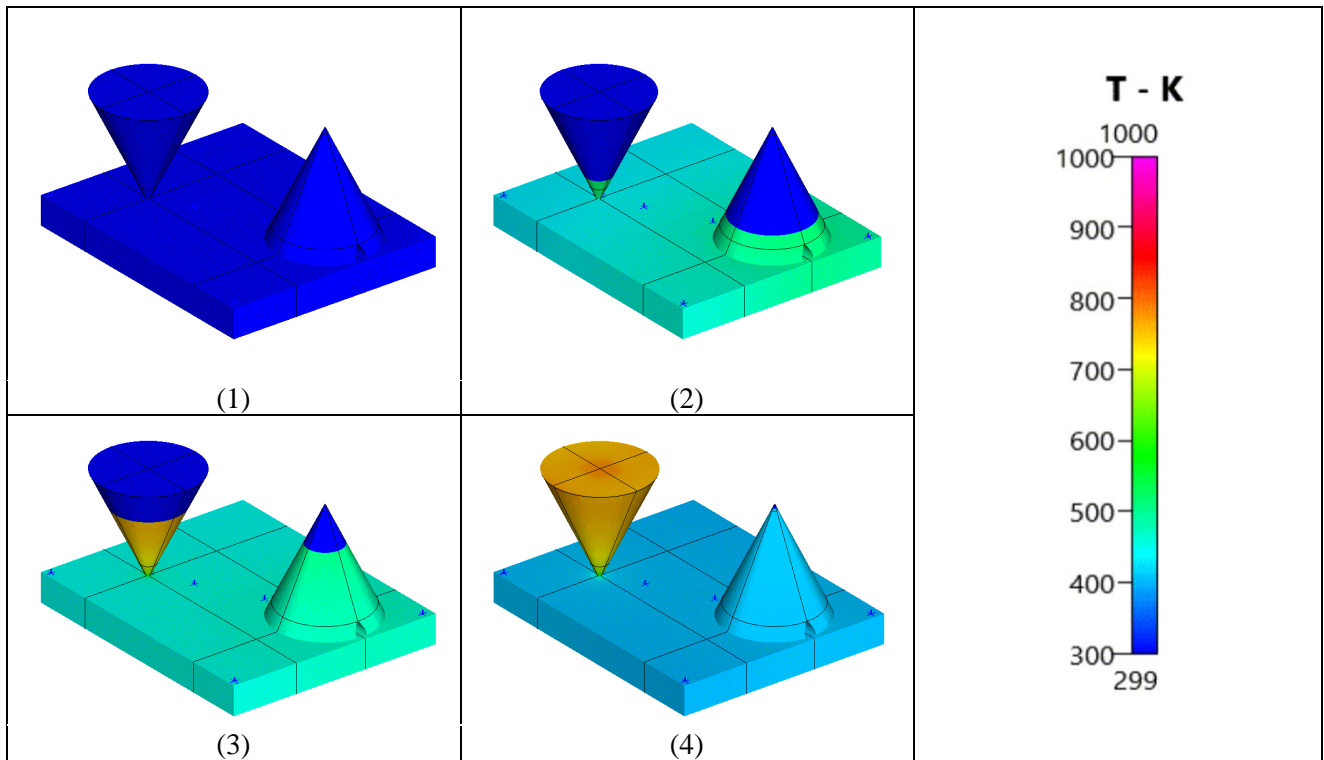
Figure 9. Numerical prediction of the overall temperature evolution in the inverted and standing cones.
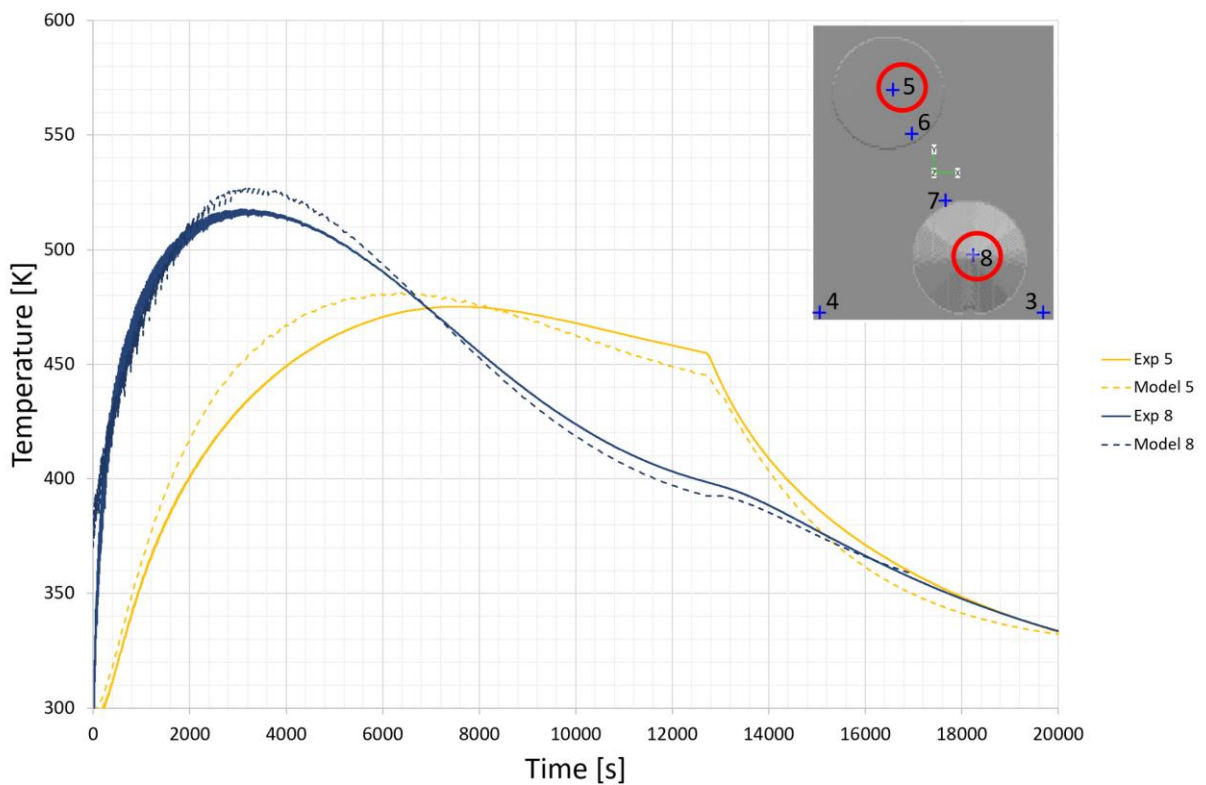
Figure 10. Comparison of measured and numerically predicted temperatures at positions 5 and 8 (red circles in top view of build).

During the heating up stage (up to 4000 s for point 8) the temperature history shows many localized peaks and valleys as the laser moves back and forth around the thermocouple/monitor point. Figure 11

zooms the heat-up period (200–400 s). The model captures the heating and cooling cycles accurately both in time and temperature magnitude. The thermal oscillations are not visible for point 5. This is attributed to the distance between the processed area, which is very small at this stage, and the thermocouple/monitor point.
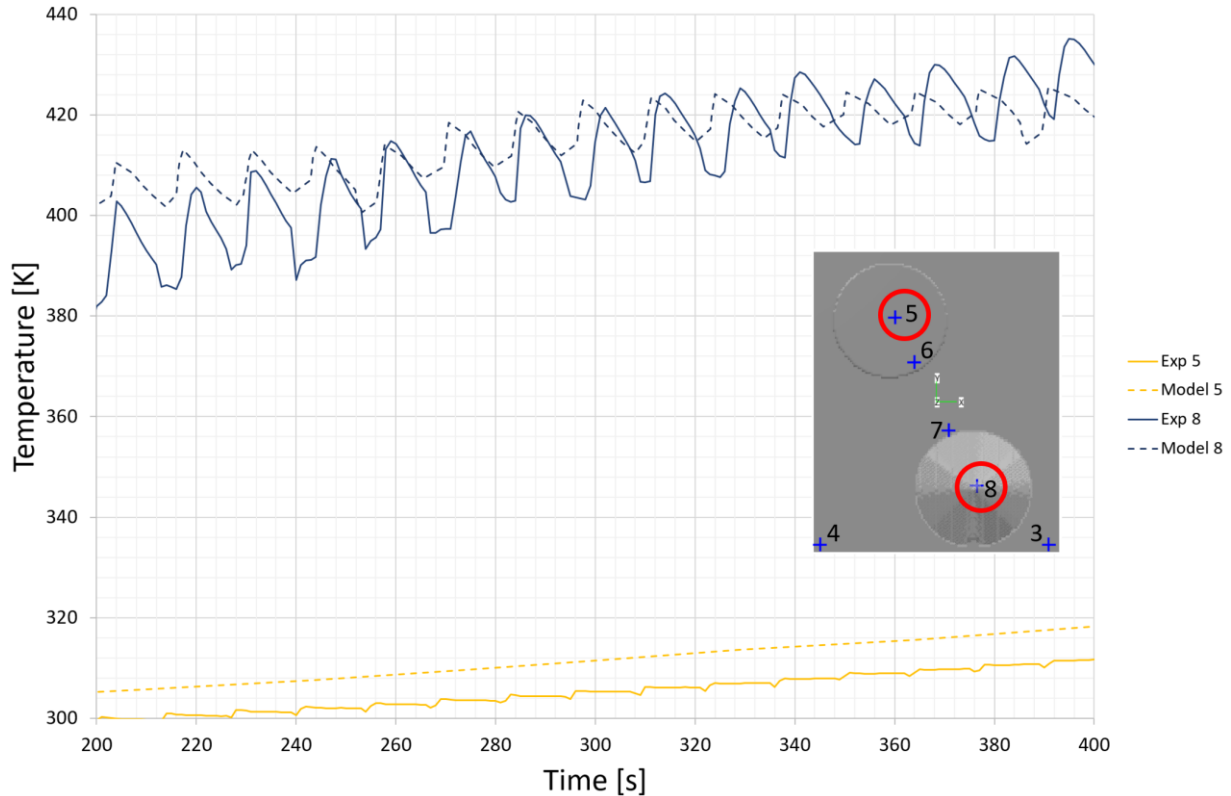
Figure 11. Zoomed thermal history during for thermocouples/monitor points 5 and 8.

Other thermocouple/monitor point results are compared in Figure 12. The good qualitative agreement between thermocouple readings and model predictions is quantified by calculating the root mean square error for all curves. The maximum root mean square error in temperature predictions is 27 K. The cooling rate after 6000 s seems to be slightly over predicted by the model. This is attributed to possible discrepancies between the applied boundary conditions and those actually found in the experiment. In the model, we assume that the powder surrounding the base plate has the same effective conductivity as the powder layer being processed. During the experiment, however, the powder was distributed manually in the based plate adapter. The base plate was placed and levelled manually prior to fixing it in place. This manual step might have led to gas enclosures below the base plate (powder distribution in the mounting frame) effectively isolating the base plate stronger than assumed. With no means to quantify this possible defect and given the general good agreement of the results, the discrepancy was considered acceptable.

Given the validated model results, we can proceed to explore the 3D domain and the thermal histories within the cones. Towards that end, four monitor points are chosen as schematically shown in Figure 13 for detailed analysis. The points of choice are placed along the cones' centre lines at $Z = 5$ mm and 30 mm.
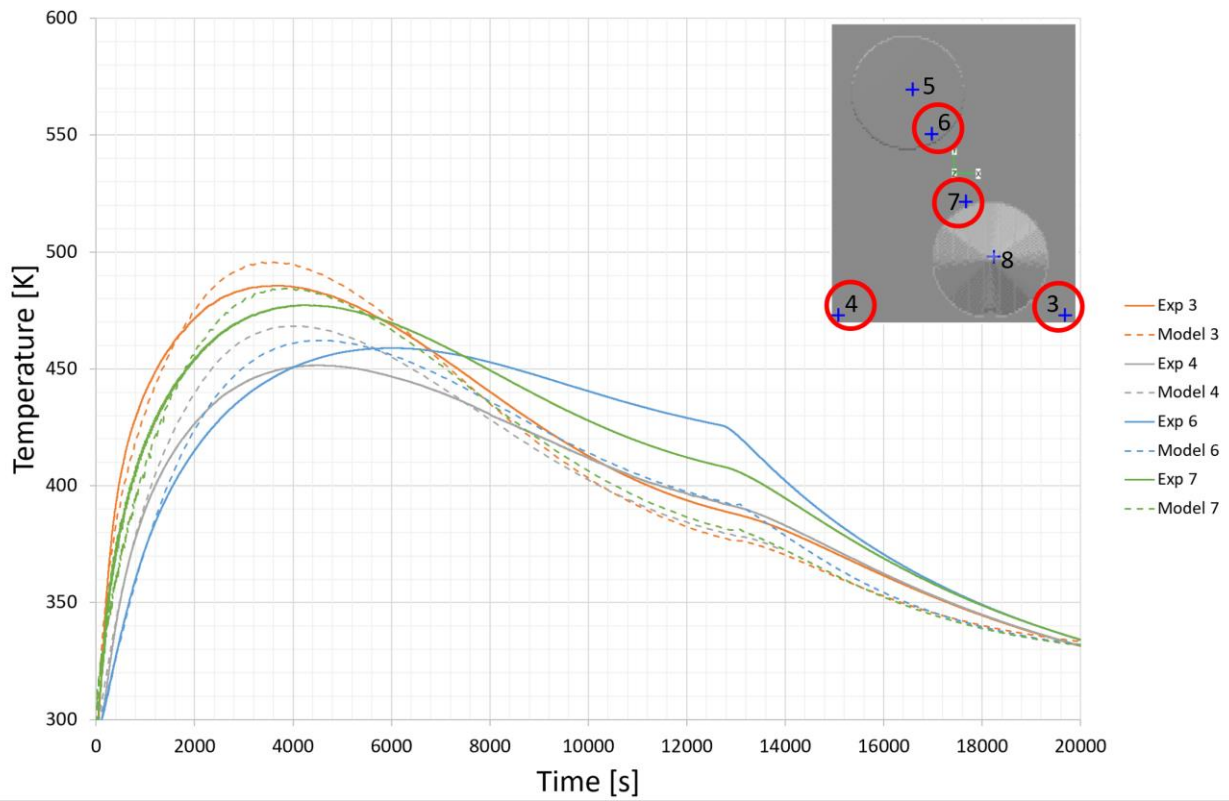
Figure 12. Comparison of measured and numerically predicted temperatures at positions 3, 4, 6 and 7 (red circles in top view of build).
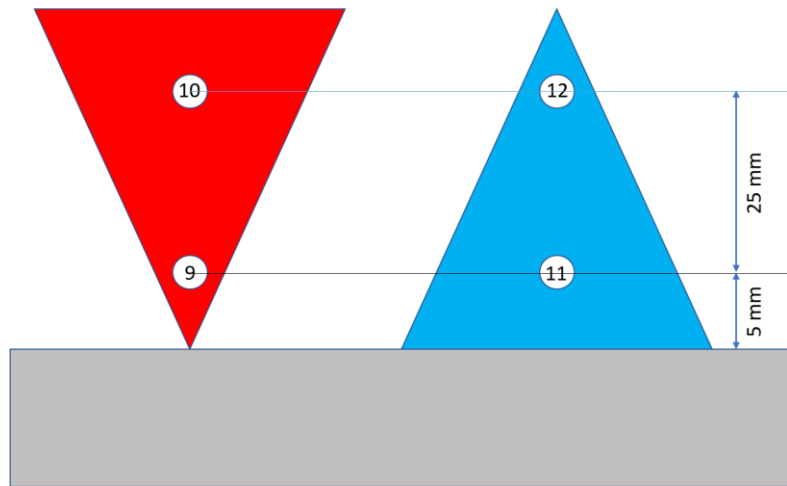
Figure 13. Exploratory points to investigate the influence of different thermal histories within one build on material property distribution.

The temperature plots for the monitor points placed along the cones' centre lines are compared in Figure 14 showing how different thermal histories are. The solidus and liquidus temperatures are included to differentiate periods where melting and solidification occur and periods where intrinsic heat treatment might occur. Monitor point 11 in the standing cone cools down to temperatures close to atmospheric conditions after the vicinity of that point is processed (after ca. 2200 s). This behavior is expected due to the sufficiently large interface area to the base plate, that functions as a heat sink. Point

9 in the inverted cone shows the same preliminary peaks attributed to the laser processing of that region, a similar cooling down to approximately atmospheric conditions due to proximity to the base plate and the ability to dissipate the limited amounts of energy required to process the cone tip, and then a continuous increase of the temperature until a plateau at 1100 K is reached and maintained for a duration of approximately 3900 s (65 minutes). The increase in energy accumulation is a result of the increased amount of energy used to process the increasing cone cross sectional area and the limited interface area between the inverted cone and the base plate.

It can be thus deduced that point 11 composition will correspond to that after rapid solidification but point 9 will undergo some intrinsic solid state transformation as discussed below.
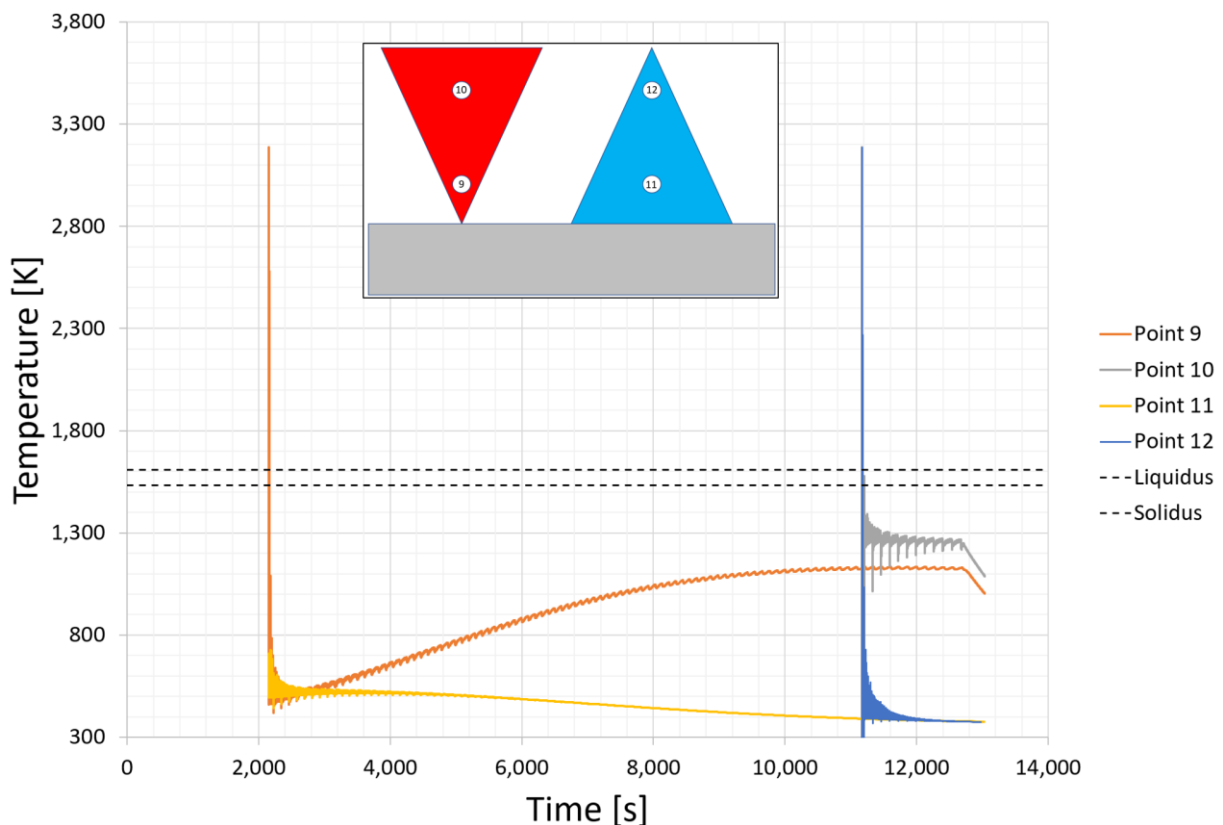
Figure 14. Thermal history at monitor points on cones' centre lines at Z = 5 mm and 30 mm above base plate surface.

Zooming into the thermal history of monitor point 9 (Figure 15a), we see that the material is melted twice, as is the case for all points considered here. Zooming further into the second solidification cycle (Figure 15b) we can quantify the cooling rate to be 1.52e6 K/s, which is very similar to the value obtained for point 11. The reason for this similarity is the proximity of those points to the base plate and the comparable thermal energy and gradients available in the system at that time. The cooling rates predicted are also in line with those reported in literature (see for example [35,36]).

Points 10 and 12, on the other hand, are processed towards the end of the build and as such the initial temperature of those curves depends on the energy accumulated in the cones considered. Point 12, which generally behaves in a similar manner to points 9 and 11, exhibits a reduced cooling rate of 3.8e5 K/s. This reduction of cooling rate is attributed to the generally lower temperatures in the vicinity of point 12 and the larger distance between point 12 and the base plate (heat sink). Independent of this decrease in

cooling rate, we still consider this value as an indicator of continued good heat dissipation throughout the build process of the standing cone and conclude that for the standing cone, there should not be a major difference in as-built material composition or mechanical properties resulting from the identified difference in cooling rate between top and bottom of the geometry.

Point 10 however is affected by the accumulation of heat in the inverted cone, that the thermal history of that point starts at approximately 1300 K and is maintained at that level for the rest of the build process (1570 s / ~26 min), see Figure 14. The predicted cooling rate at point 10 is 7.6e5 K/s, twice as high as that of point 12. The distance to the heat sink is identical and the difference is solely due to the difference in temperature gradients. We thus conclude that for the inverted cone, cooling rates have the same order of magnitude as in the standing cone, but high temperatures are maintained so that post solidification phase transformations may lead to different compositions from bottom to top of the cone.
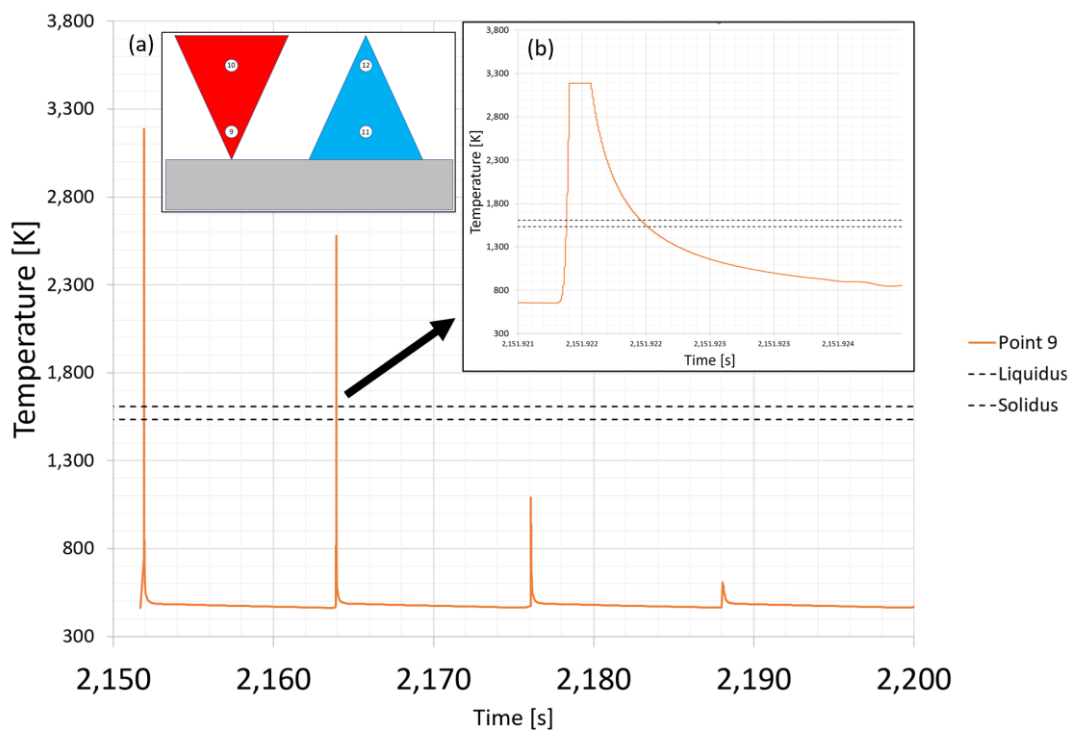
Figure 15. **(a)** Number of remelts at monitor point 9. **(b)** Cooling curve of second solidification cycle.

The spatial and temporal temperature distributions are transferred to a grain growth model based on the work done by Mosbah *et al.* [37] and Attard *et al.* [6]. The grain orientation in the first layer is randomly defined. Attard *et al.* found that a higher nucleation density than those expected for conventional solidification is required for additive manufacturing models to predict equiaxed grain growth [6]. A nucleation density of 11.4e15 m^{-3} is assumed in the melt pool in line with values used in [6]. The numerically predicted conduction mode melt pool shapes are comparable with those shown in Figure 7 and are shown together with the microstructures are shown in Figure 16. The first melting cycle results in equiaxed grains in the center and top of the melt pool geometry. The second melting process remelts the equiaxed grains enabling epitaxial grain growth of grains originating from the previously processed layers. Since all monitor points exhibit 2 remelts, columnar grains are expected throughout the cones, which is in general agreement with the microstructures observed for both cones shown in Figure 17. The microstructure of both cones is very similar and cannot be distinguished from one another.
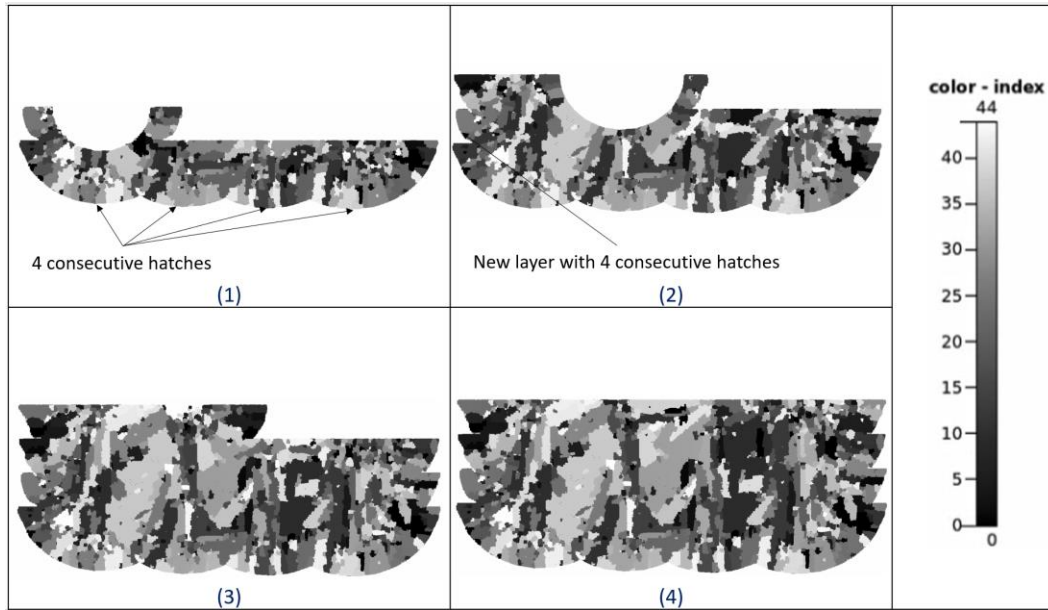
Figure 16. Temporal sequence of grain growth model shown 4 hatches and 2 remelts leading to elongated and columnar grains.
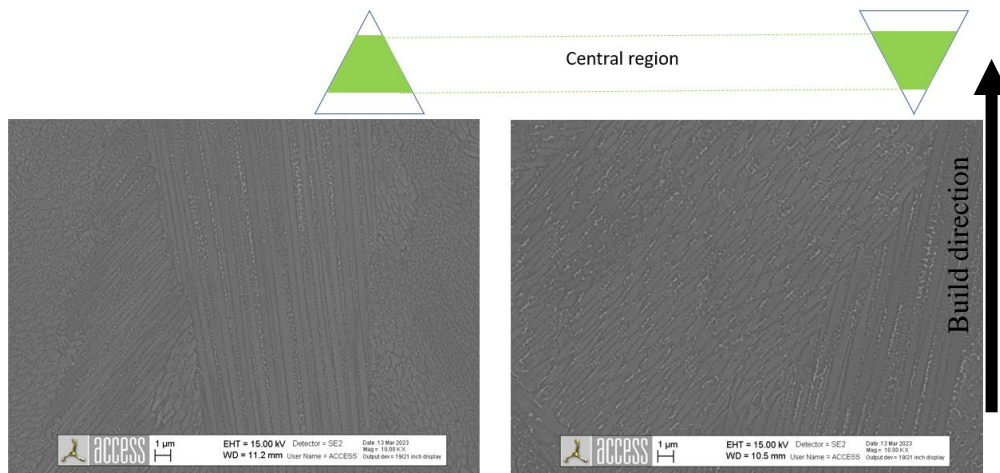
Figure 17. Microstructure in centre of both standing (left) and inverted (right) cones showing epitaxial grain growth.

All cooling rates, despite differences quantified, lead to non-equilibrium solidification conditions. The solidification curve and the as-built phase concentrations are therefore calculated using Scheil-Gulliver equation, which assumes no diffusion in solid (due to very high cooling rate) and infinite diffusion within the melt pool, which is justified by convective flows in the melt pool but will affect prediction accuracy ahead of the solidification front. Figure 18 shows the solidification curve and expected as-built phases. A diffusion analysis at point 9 (lower monitor point of inverted cone) is performed at 1100 K for a duration of 3900 s showing that no diffusion is to be expected after printing. The predicted phases are in-line with literature observations for as-built IN718, see for example [38]. Precipitation calculations are performed using the Kampmann/Wagner Numerical (KWN) model to predict the growth of to γ' and γ'' precipitates as seen in Figure 19 [39]. The TTT diagram suggests that precipitates are not to be expected for monitor point 10 (upper monitor point of inverted cone) because the temperature after printing (1300 K) is only

held for 1570 s. Points 11 and 12 are also not predicted to exhibit precipitation because the temperature held after printing is too low. For point 9, however, the precipitation model shows that γ' and γ'' particle sizes should reach sizes of up to 15 and 20 nm, respectively.

Temperature [K]		Phase Name
1611.66	1517.16	Liquid+Fcc
1517.06	14567.66	Liquid+Fcc+Fcc_MC
1467.56	1456.36	Liquid+Fcc+Fcc_MC+Laves_C14
1456.26	1421.96	Liquid+Fcc+Fcc_MC+Laves_C14+Delta
1421.86	1420.76	Liquid+Fcc+Fcc_MC+Laves_C14+Delta+M3B2
1420.66	1413.26	Liquid+Fcc+Fcc_MC+Laves_C14+Delta+M3B2+MB2
1412.86	-	Fcc+Fcc_MC+Laves_C14+Delta+M3B2+MB2
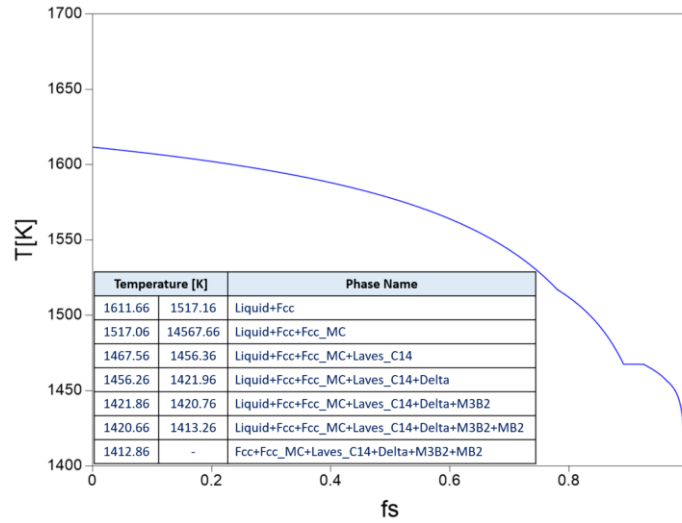
Figure 18. Scheil-Gulliver solidification curve and corresponding phases.
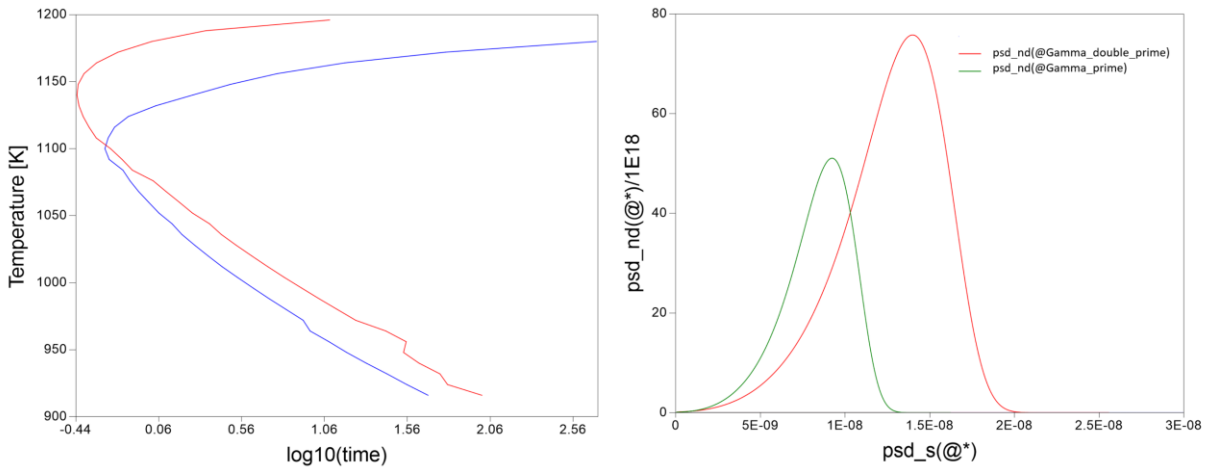
Figure 19. IN718 precipitations at monitor point 9 (lower monitor point of inverted cone): **(a)** TTT diagram, **(b)** Precipitation number density over particle size in meters.

It can be therefore deduced that two process relevant time scales are to be considered:

(1) The melt pool time scale, where thermal cycling plays an important role in determining the melt pool size. The cooling rate is usually in the order of 10^6 K/s as shown for example in Figure 15. The melt pool time scale determines the nucleation and preliminary microstructure as seen in Figure 16. When remelting equiaxed grains epitaxial growth is favored leading to columnar growth typically found in LB-PBF parts.

(2) The build time scale, where the temperatures might rise depending on the geometric features and the scan strategy as shown for example in Figure 14 for point 9. For the geometry and scan strategy studies here, point 9 heats up to about 1100 K and remains at that value for approx. 1 hour. This is comparable to heat treatment and could lead to changes in microstructure and mechanical properties as discussed below.

Vicker's hardness measurements are obtained from several points, each 1 mm apart from the next point, on the middle plane of each of the cones corroborate numerical predictions. Despite the similarity of microstructure in the center of both cones (see Figure 17), hardness measurements shown as contour plots in Figure 20a show significant differences between both cones. The standing cone seems a little smaller than the inverted cone, because of the channel required for the thermocouple wires and it generally has lower hardness values than those shown for the inverted cone. Average measurements along the cones' center lines together with standard deviations are shown in Figure 20b. The standing cone shows lower hardness values with higher standard deviations and non-uniform values along the building direction—the values decreasing with build height. The inverted cone on the other hand shows higher hardness values, almost constant along building direction with lower standard deviations. The average hardness measured for the inverted cone is 339 HV *versus* 309 HV for the standing cone.
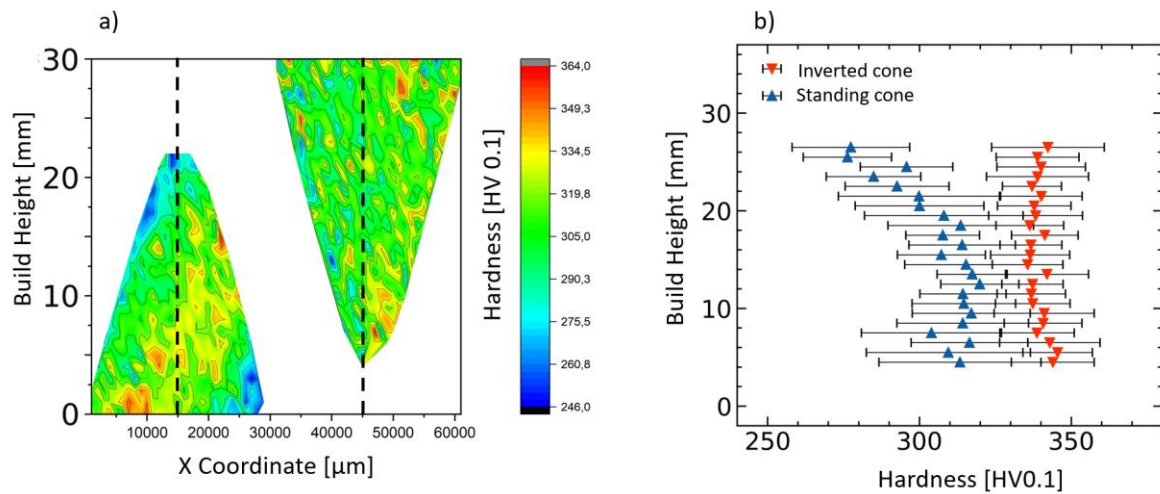
Figure 20. (a) Contour plot of measured Vickers hardness at multiple points on middle plane of IN718 cones. **(b)** Average Vickers hardness along centre line of standing and inverted cones and corresponding standard deviation.

The increased hardness in lower regions of inverted cone is attributed to γ' and γ''precipitations numerically predicted as discussed above. This is also in agreement with the findings of Rielli *et al.* [40], where short durations at approx. 1000 K were found to be sufficient to significantly increase IN718 hardness via γ' and γ''precipitations. The reduction of hardness in the upper regions of the standing cone indicates that there are other processes in play that affect the mechanical properties. It is assumed that the cooling rate decreases with build height leading to larger grains and lower hardness in the upper regions of the standing cone. In the case of the inverted cone, however, the increase in cone cross section leads to higher processing temperatures (see Figure 8) leading to higher a cooling rate and increased hardness. A more detailed analysis of the microstructure in upper regions is planned for future investigations to corroborate these assumptions.

The contour plots of the inverted cone show a more uniform hardness distribution. The standard deviation of inverted cone is 13.6 HV compared to 21.4 HV for the standing cone. This is attributed to the high and uniform temperature held throughout the build process in the inverted cone for a relatively long time (3900 s), which leads to an intrinsic heat treatment leading to precipitation hardening in the lower regions and smaller grains in the upper regions. The standing cone in contrast seems to have a

diagonal from the lower left side, where the thermocouple channel ends to the top right cone boundary, showing higher hardness values. The reason for this behavior could not be identified.

The thermal model is qualitatively verified using online thermal cameras as well as quantitatively validated using thermocouples. The results show that all probes investigated in detail undergo at least 2 remelting cycles. Non-equilibrium solidification is always to be expected. The model captures and quantifies the thermal conditions pertinent for material evolution after it has been deposited. As heat accumulates in the build, melt pool dimensions change and solid-state transformations may occur leading to different microstructures and property distribution throughout the build. The model has been successfully applied to support microstructural design (see for example [6]) and identifying morphology and surface defects (see for example [24]) thus closing the gap between process chain models and material models. In doing so the computational effort of the 3D thermal model is comparable with the effort required for CALPHAD calculations performed to explore points of interest in the build as well as grain growth models. It does, however, rely on the availability of scan path files, that describe the laser trajectory and corresponding process parameter changes (e.g., bulk *versus* contour scans). Whereas this information is available for us using open machines, it remains a challenge when modelling the processes taking place in many commercial L-PBF printers. To circumvent this short coming the authors are researching methods to relax this requirement, which a possible drawback of reduced fidelity when designing as-built microstructures.

5. Summary and conclusions

In this study, a semi-analytic thermal model is validated, that resolves all laser scans to provide high resolution thermal histories for 3D L-PBF parts. The result can be explored using readily available simulation post processors to identify regions and points of interest that can be further analyzed in detail. The local thermal histories provide approximate melt dimensions (neglecting melt pool dynamics), which is used to drive grain growth models enabling prediction of microstructures and their design. Temporal and thermal conditions after deposition are quantified, such that CALPHAD calculations can be used to predict phase concentrations and variations in as-built properties. The computational effort of the thermal model is comparable with that of multiple CALPHAD calculations exploring 4–5 points of interest throughout the build thus presenting a tool linking process modelling with ICME efficiently.

An experimental setup was designed to control thermal boundary conditions in a more accurate manner for this validation work. Scaling of the cones is straight forward and would allow for the generation of several variants of the thermal histories discussed here presenting a larger data set for ICME model validation and exploration of new scan strategies. For real life applications, where the base plate is connected to printer's metallic structure, the model might need to be extended to resolve the larger structure and corresponding thermal boundary conditions.

The modelling chain presented here accounts for the scan file used in the printer, the thermal history of the part printed, phase transformation modelling and microstructure growth models. IN718 was chosen for this pilot study due to the large bulk of data pertaining to LB-PBF of IN718. The simple benchmark geometry was chosen to highlight the influence of geometric features on the thermal history and the evolution of as-built material properties. Future work will continue to rely on this simple geometry, possibly scaling it to enlarge the difference in thermal histories to explore other alloys and alternative scan strategies. Whereas the results are expected to be less relevant for industrial application,

they will provide a foundation for judging thermal histories, gradients and alloy specific models. In parallel to process and metallurgical studies there remains need for numerical improvements to relax or eliminate limitations discussed above such as the modelling of multi-laser printing and beam shaping.

Acknowledgement

Authors' contribution

Conceptualization, M.M., M.V. and S.V.; methodology, M.M.; software, P.D.; validation, M.M., and P.D.; formal analysis, M.V. and M.M.; investigation, M.V.; resources, S.V.; data curation, M.M.; writing—original draft preparation, M.M.; writing—review and editing, M.V., S.V. and P.D.; visualization, M.M.; supervision, M.M.; project administration, S.V.; funding acquisition, S.V. All authors have read and agreed to the published version of the manuscript.

Conflicts of interests

Simon Vervoort and Mustafa Megahed declare that financial support was provided by federal Ministry of Economic and Environment Protection. All authors declare that they have no known competing financial or personal relationships that could have appeared to influence the work reported in this paper.

References

[1] Liu F, Lin X, Huang C, Song M, Yang G, *et al.* The effect of laser scanning path on microstructures and mechanical properties of laser solid formed nickel-base superalloy Inconel 718. *J. Alloys Compd.* 2011, 509(13):4505–4509.

[2] Körner C, Helmer H, Bauereiß A, Singer RF. Tailoring the grain structure of IN718 during selective electron beam melting. *MATEC Web Conf.* 2014, 14:08001.

[3] Popovich VA, Borisov EV, Popovich AA, Sufiiarov VS, Masaylo DV, *et al.* Functionally graded Inconel 718 processed by additive manufacturing: Crystallographic texture, anisotropy of microstructure and mechanical properties. *Mater. Des.* 2017, 114:441–449.

[4] Keshavarzkermani A, Sadowski M, Ladani L. Direct metal laser melting of Inconel 718: Process impact on grain formation and orientation. *J. Alloys Compd.* 2018, 736:297–305.

[5] Zhang C, Chen F, Huang Z, Jia M, Chen G, *et al.* Additive manufacturing of functionally graded materials: A review. *Mater. Sci. Eng. A* 2019, 764:138209.

[6] Attard B, Cruchley S, Beetz C, Megahed M, Chiu YL, *et al.* Microstructural control during laser powder fusion to create graded microstructure Ni-superalloy components. *Addit. Manuf.* 2020, 36:101432.

[7] Nadammal N, Mishurova T, Fritsch T, Serrano-Munoz I, Kromm A, *et al.* Critical role of scan strategies on the development of microstructure, texture, and residual stresses during laser powder bed fusion additive manufacturing. *Addit. Manuf.* 2021, 38:101792.

[8] Wei HL, Mazumder J, DebRoy T. Evolution of solidification texture during additive manufacturing. *Sci. Rep.* 2015, 5(1):16446.

[9] Rai A, Helmer H, Körner C. Simulation of grain structure evolution during powder bed based additive manufacturing. *Addit. Manuf.* 2017, 13:124–134.

[10] Mindt HW, Desmaison O, Megahed M, Peralta A, Neumann J. Modeling of Powder Bed Manufacturing Defects. *J. Mater. Eng. Perform.* 2018, 27(1):32–43.

[11] Panwisawas C, Qiu C, Anderson MJ, Sovani Y, Turner RP, *et al.* Mesoscale modelling of selective laser melting: Thermal fluid dynamics and microstructural evolution. *Comput. Mater. Sci* 2017, 126:479–490.

[12] Koepf JA, Gotterbarm MR, Markl M, Körner C. 3D multi-layer grain structure simulation of powder bed fusion additive manufacturing. *Acta Mater.* 2018, 152:119–126.

[13] Rosenthal D. The Theory of Moving Sources of Heat and Its Application to Metal Treatments. *Trans. ASME.* 1946, 68(8):849–865.

[14] Eagar T, Tsai N. Temperature fields produced by traveling distributed heat sources. *Welding J.* 1983, 62(12):346–355.

[15] Kamath C, El-dasher B, Gallegos GF, King WE, Sisto A. Density of additively-manufactured, 316L SS parts using laser powder-bed fusion at powers up to 400 W. *Int. J. Adv. Manuf. Technol.* 2013, 74(1):65–78.

[16] Tang M, Pistorius PC, Beuth JL. Prediction of lack-of-fusion porosity for powder bed fusion. *Addit. Manuf.* 2017, 14:39–48.

[17] Prisco U. Shape of the melt pool produced by a moving Gaussian heat source. *Weld. World* 2021, 65(11):2105–2118.

[18] Whalen BJ, Ma J, Balachandran PV. A Bayesian Approach to the Eagar-Tsai Model for Melt Pool Geometry Prediction with Implications in Additive Manufacturing of Metals. *Integr. Mater. Manuf. Innov.* 2021, 10(4):597–609.

[19] Hann DB, Iammi J, Folkes J. A simple methodology for predicting laser-weld properties from material and laser parameters. *J. Phys. D: Appl. Phys.* 2021, 44:445401.

[20] Wayne EK, Barth HD, Castillo VM, Gallegos GF, Gibbs JW, *et al.* Observation of keyhole-mode laser melting in laser powder-bed fusion additive manufacturing. *J. Mat. Proc. Tech.* 2014, 214(12):2915–2925.

[21] Hanemann T, Seyfert C, Holfelder P, Rota A, Heilmaier M. Dimensionless enthalpy as characteristic factor for process control in laser powder bed fusion. *J. Laser Micro Nanoen.* 2020, 15(3):257–266.

[22] Liu B, Fang G, Lei L. An analytical model for rapid predicting molten pool geometry of selective laser melting (SLM). *Appl. Math. Mod.* 2021, 92:505–524.

[23] Ji X, Wang Y, Liang SY. Analytical modeling of temperature evolution in laser powder bed fusion considering the size and shape of the build part. *J. Mat. Proc. Tech.* 2022, 301:117452.

[24] Duong E, Masseling L, Knaak C, Dionne P, Megahed M. Scan path resolved thermal modelling of LPBF. *Addit. Manuf. Lett.* 2022, 3:100047.

[25] Moran TP, Warner DH, Phan N. Scan-by-scan part scale thermal modelling for defect prediction in metal additive manufacturing. *Addit. Manuf.* 2021, 37:101667.

[26] Wolfer AJ, Aires J, Wheeler K, Delplanque JP, Rubenchik A, *et al.*, Fast solution strategy for transient heat conduction for arbitrary scan paths in additive manufacturing. *Addit. Manuf.* 2019, 30:100898.

[27] Wang ZJ, Srinivasan K. An adaptive Cartesian grid generation method for 'dirty' geometry. *Int. J. Numer. Meth. Fluids.* 2002, 39:703–717.

[28] Common Layer Interface (CLI) version 2.0. Available: https://www.hmilch.net/downloads/cli_for mat.html?trk=public_post_comment-text (accessed on 17 April, 2018).

[29] Kramer T, Proctor F, Messina E. The NIST RS274NGC Interpreter - Version 3. NIST Interagency/Internal Report (NISTIR), National Institute of Standards and Technology, Gaithersburg. Available: http://www.nist.gov/manuscript-publicationsearch.cfm?pub_id=823374 (accessed on 17 April 2018).

[30] Sainte-Catherine C, Jeandin M, Kechemair D, Ricaud JP, Sabatier L. Study of dynamic absorptivity at 10.6 µm (CO2) and 1.06 µm (Nd-YAG) wavelengths as a function of temperature. *J. Phys. IV France* 1991, 01(C7):C7–151–C157–157.

[31] Hosaeus H, Seifter A, Kaschnitz E, Pottlacher G. Thermophysical properties of solid and liquid inconel 718 alloy. *High Temp.-High Pressures* 2001, 33:405–410.

[32] Pottlacher G, Hosaeus H, Wilthan B, Kaschnitz E, Seifter A. Thermophysikalische Eigenschaften von festem und flüssigem Inconel 718. *Thermochim. Acta* 2002, 382(1–2):255–267.

[33] Cao L, Yuan X. Study on the numerical simulation of the SLM molten pool dynamic behavior of a nicker-based superslloy on the workpiece scale. *Materials* 2019, 12(14): 2272.

[34] Wei LC, Ehrlich LE, Powell-Palm MJ, Montgomery C, Beuth J, *et al*. Thermal conductivity of metal powders for powder bed additive manufacturing. *Addit. Manuf.* 2018, 21:201–208.

[35] Hooper PA. Melt pool temperature and cooling rates in laser powder bed fusion. *Addit. Manuf.* 2018, 22:548–559.

[36] Panwisawas C, Tang YT, Ghoussoub J, Reed RC. Additive manufacturability of Nickl-based superalloys: Composition-process induced vapourization. In *Superalloys 2020*, Cham: Springer, 2020. pp. 1024–1032

[37] Mosbah S. Grain structure and segregation modeling using coupled FV and DP model. In *8th International Symposium on Superalloy 718 and Derivatives*, Pennsylvania, USA, September 28– October 1, 2014, pp. 237.

[38] Sanchez S, Smith P, Xu Z, Gaspard G, Hyde CJ, *et al*. Powder bed fusion of nickel-based alloys: A review. *Int. J. Mach. Tools Manuf.* 2021, 165:103729.

[39] Ury N, Neuberger R, Sargent N, Xiong W, Arroyave R, *et al*. Kawin: An open source Kampmann-Wagner Numerical (KWN) phase precipitation and coarsening model. *Acta Mater.* 2023, 255:118988.

[40] Rielli VV, Theska F, Godor F, Stanojevic A, Oberwinkler B, and *et al*. Evolution of nanoscale precipitates during common alloy 718 ageing treatments. *Mater. Des.* 2021, 205:109762.